

Article

# Correlation of Near-Inertial Wind Stress in Typhoon and Typhoon-Induced Oceanic Near-Inertial Kinetic Energy in the Upper South China Sea

Juan Li <sup>1,2</sup>, Jiexin Xu <sup>1</sup> , Junliang Liu <sup>1</sup>, Yinghui He <sup>1</sup>, Zhiwu Chen <sup>1</sup> and Shuqun Cai <sup>1,3,\*</sup>

<sup>1</sup> State Key Laboratory of Tropical Oceanography, South China Sea Institute of Oceanology, Chinese Academy of Sciences, Guangzhou 510301, China

<sup>2</sup> University of Chinese Academy of Sciences, Beijing 100049, China

<sup>3</sup> Institution of South China Sea Ecology and Environmental Engineering, Chinese Academy of Sciences, Guangzhou 510301, China

\* Correspondence: caisq@scsio.ac.cn; Tel.: +86-20-89023186

Received: 10 June 2019; Accepted: 9 July 2019; Published: 11 July 2019



**Abstract:** The correlation of near-inertial wind stress (NIWS) in typhoon and typhoon-induced oceanic near-inertial kinetic energy (NIKE) in the upper South China Sea (SCS) is investigated through reanalysis data and an idealized typhoon model. It is found that the typhoon-induced oceanic near-inertial currents are primarily induced by the NIWS, which may contribute to about 80% of the total NIKE induced by typhoon. The intensities and distributions of NIWS in most typhoons are consistent with the magnitudes and features of NIKE. The NIWS and the NIKE along the typhoon track have positive correlations with the maximum wind speed of a typhoon, but there is an optimal translation speed for NIWS, at which the wind energy of the near-inertial band reaches its maximum. In the idealized typhoon model, a cluster of high-value centers of NIWS appear along the typhoon track, but there is only one high-value center for the near-inertial currents. The maximum NIWS arrives about 15 hours prior to the maximum near-inertial current. The distribution of NIWS is apparently asymmetric along the typhoon track, which may be due to the smaller eastward component of wind energy.

**Keywords:** near-inertial wind stress; near-inertial kinetic energy; typhoon; South China Sea

## 1. Introduction

Winds are the major mechanical energy source for driving the large-scale ocean circulation and the abyssal mixing in the ocean. Previous studies estimated that nearly 2.1 TW (Terawatts) were required to maintain the global general circulation in the ocean and approximately 1–1.2 TW from winds available for interior mixing [1–4]. Although wind power input is the major mechanical energy source, most of the wind input energy is dissipated when propagating downwards. However, a significant part of oceanic near-inertial energy, which is mainly generated by variable wind stress, can propagate into the deep ocean for diapycnal mixing and meridional overturning circulation [5–10]. The strong atmospheric force excited by the passages of tropical cyclones can motivate strong near-inertial motions in the upper ocean. It is estimated that there is about 0.03 TW of near-inertial energy induced by tropical cyclones in the global ocean [11]. Hence, it is an important energy source to the ocean where tropical cyclones frequently visit or generate.

It is known that tropical cyclones are the extreme products of air–sea interaction and can generate vigorous responses in the open ocean. The oceanic response to the passages of tropical cyclones has two stages, including a forced stage and a relaxation stage [5]. The forced stage response is mostly local, including surface waves higher than 20 m, sea surface temperature cooling of several degrees,

and more than 1 m/s enhanced upper ocean currents [12]. The time scale of a forced stage response is the storm residence time (typically half a day). The relaxation stage is an inherently nonlocal baroclinic response, including the near-inertial internal waves penetrating the thermocline, and the time scale is typically 5–10 days [13].

Tropical cyclones vary with respect to size (e.g., the radius of maximum winds), intensity, translation speed, maximum wind speed, asymmetries, location, etc. [14]. The typhoon-induced oceanic near-inertial motions are always confined to some independent parameters of the preceding typhoon, e.g., wind speed, translation speed, spatial scale, and other parameters, e.g., Coriolis parameter  $f$ , the oceanic stratification [15–17]. Nilsson [17] proposed that the internal wave power induced by traveling hurricanes generated from the divergence of wind stress and the curl of wind stress. The former part of the energy depends on the speed of the hurricane. For a specified stratification and fixed latitude, the maximum of the internal wave power always presents an optimal turn with the speed of the hurricane. Chen et al. [18] subsequently pointed out that the oceanic near-inertial response arises when the wind speed increases or with a closer frequency to the inertial frequency at a fixed point. Meanwhile, the amplitude of oceanic inertial oscillation increases with increasing translation speed, due to the higher local rotation frequency, but a faster cyclone has shorter influence duration, which may lead to less oceanic near-inertial energy induced in the ocean.

In the northern hemisphere, the wind stress of tropical cyclones is always larger on the right side of the track, which arises from many factors [19], e.g., the translation speed [20], friction [21], vertical shear and environmental conditions [22], and the beta effect [23]. The oceanic inertial oscillation is also much stronger on the right side of the storm path than the left side in the northern hemisphere. The rightward bias is usually attributed to the resonance effect via the air–sea interactions, i.e., the wind stress vectors on the right (or left) of the cyclone track turn clockwise (or anticlockwise) and resonate with typhoon-generated oceanic currents, resulting in more (or less) intensive kinetic energy generated in the upper ocean. When the rotation rate of resonant near-inertial oceanic currents matches the local inertial frequency, the maximal amplitude of inertial oscillations is generated [18,24,25].

The South China Sea (SCS) is the largest marginal sea in the Western Pacific. Due to its special geographical location, the SCS is subject to the frequent tropical cyclone activity, and the mature tropical cyclone is also called a typhoon in the Northwest Pacific. There are about 15 tropical cyclone visits, or cyclogenesis, every year in the SCS [15]. As a frequently visited tropical cyclone area, the oceanic response to typhoons in the SCS attracts more attention, and the typhoon-induced near-inertial motions are often investigated by mooring observational data or numerical models [26–31]. For example, in the northern SCS, a strong near-inertial bottom current (about 80 m depth) was observed during the passage of Typhoon Pabuk, which was comparable to the upper-layer near-inertial current [32]. On the shelf (60 m deep) of the northern SCS, it was observed that there are two spectral peaks at sub-inertial and super-inertial frequencies with two boundaries at 17 and 40 m, respectively, where the near-inertial energy is reflected upward and downward when the typhoon passed [24]. The oceanic near-inertial kinetic energy (NIKE) was observed to be significantly enhanced by a factor of 10 during the passage of Typhoon Hagupit [8]. Some observations also show that the behavior of different typhoon-induced near-inertial motions may be determined by typhoon disturbance, the background ocean condition [15], and translation speed [33].

However, typhoon-induced oceanic near-inertial motions vary with different typhoon characteristics and ocean conditions. The underlying dynamic mechanisms of the typhoon-induced oceanic near-inertial motions and the relationship between oceanic near-inertial motions and typhoon parameters are not very clear. According to previous studies, the wind stress at frequencies close to the local inertial frequency is most effective in exciting near-inertial motions in the ocean [34,35]. Investigating near-inertial wind stress (NIWS) in typhoons would be a key point to understand the relationship between typhoons and oceanic near-inertial motions, and explore further possible mechanisms in consideration of different parameters of typhoons aforementioned. Therefore, the paper is organized as follows: In Section 2, we describe the details of the data and calculation methods used

in this study. In Section 3, the relationships among some parameters of typhoons, typhoon-induced oceanic near-inertial motions, and NIWS in typhoons are investigated and analyzed. Finally, a summary is provided in Section 4.

## 2. Data and Processing Methodology

### 2.1. Typhoons and Meteorological Observation in the SCS

Time series of observed wind data are measured by a meteorological sensor at an interval of 120 s at the meteorological observation station of Xisha Islands (16°83' N, 112°33' E) from 6 April to 31 December in 2008 (marked by black pentagram in Figure 1).

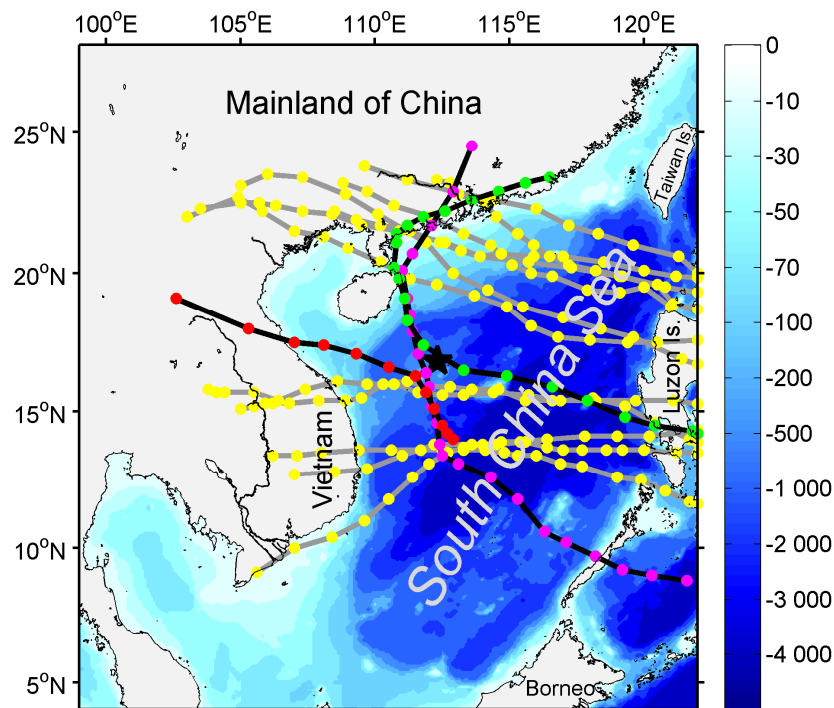


**Figure 1.** Bathymetry of the South China Sea (unit in m), the position of meteorological sensor (black pentagram) and 15 typhoons from 2001 to 2009. The tracks of typhoons Neoguri, Mekkhala, and Higos are denoted by magenta, red, and green dots, respectively. The trajectories of typhoons Yutu, Molave, Nuri, Koppu, Imbudo, Krovanh, Hagupit, Xangsane, Ketsana, Mirinae, Lingling, and Durian are denoted by yellow dots.

### 2.2. Typhoon Data and Atmospheric Forcing

The intensity and track of tropical cyclones used in this study are provided by the China Meteorological Administration (CMA)'s TC database [36].

The wind fields of 12 typhoons come from the hourly National Centers for Environmental Prediction (NCEP) Climate Forecast System Reanalysis (CFSR) [37], which have a fine spatial and temporal resolution (hourly and  $0.5^\circ \times 0.5^\circ$ ). The wind stress can be calculated from the formula:

$$(\tau_x, \tau_y) = \rho_a C_d \sqrt{u_{10}^2 + v_{10}^2} (u_{10}, v_{10}), \quad (1)$$

where  $\rho_a$  is the air density (we take  $1.3 \text{ kg m}^{-3}$  here);  $U_{10} = (u_{10}, v_{10})$  is the wind speed at 10 m height from the sea surface; and  $C_d$  is the drag coefficient. To get more valid wind stress, we follow Oey et al. [38], and the  $C_d$  is adopted as [33,39],

$$C_d = \begin{cases} 1.2 \times 10^{-3}, & U_{10} \leq 11 \text{ m/s} \\ (0.49 + 0.065U_{10}) \times 10^{-3}, & 11 < U_{10} \leq 19 \text{ m/s} \\ (1.364 + 0.0234U_{10} - 0.0002U_{10}^2) \times 10^{-3}, & 19 < U_{10} \leq 100 \text{ m/s} \end{cases} \quad (2)$$

which fits the formula proposed by Large and Pond [40] for low-to-moderate wind speeds and by Powell et al. [41] for high wind speeds. Then, the Butterworth band-pass filter with a frequency range of  $0.85\text{--}1.15f$  [28] is applied to wind stress in getting the NIWS. The magnitude of NIWS can be defined by [42],

$$NIWS = \sqrt{\tau_{x,i}^2 + \tau_{y,i}^2} \quad (3)$$

where  $\tau_{x,i}$  and  $\tau_{y,i}$  are the two components of NIWS.

### 2.3. Slab Model

Here, a simple one-dimensional slab model of Pollard and Millard [43] is used to simulate the oceanic near-inertial response to wind stress within the mixed layer. The model equations are as follows,

$$\begin{cases} \frac{du}{dt} - fv = \frac{\tau_x}{H\rho_0} - ru, \\ \frac{dv}{dt} + fu = \frac{\tau_y}{H\rho_0} - rv, \end{cases} \quad (4)$$

where  $u$  and  $v$  are the eastward and northward components of near-inertial currents;  $\tau_x$  and  $\tau_y$  are the eastward and northward components of surface wind stress;  $\rho_0 = 1024 \text{ kg m}^{-3}$  is the density of sea water;  $r$  is the damping coefficient, and here it is taken as  $0.15f$ , according to Alford [44].  $H$  is the mixed layer depth, which is defined as the depth where the temperature is  $0.5 \text{ }^\circ\text{C}$  less than the sea surface temperature (SST) [45], and the water temperature comes from the global  $1/12^\circ$  reanalysis product of the Hybrid Coordinate Ocean Model (HYCOM) and the Navy Coupled Ocean Data Assimilation (NCODA) reanalysis data [46–48]. Although the slab model is only a local single-point model and does not fully represent the inertial processes, e.g., propagation between points at nearby positions is not allowed, and only local processes are considered, it can generate well-matched near-inertial oscillations with observation in the mixed layer [18,44,49].

Then the NIKE can be calculated by

$$NIKE = \frac{1}{2}\rho_0(u^2 + v^2), \quad (5)$$

where  $u$  and  $v$  are the eastward and northward components of near-inertial current  $U_i$ .

### 2.4. Current Data

To further examine the oceanic near-inertial currents induced by typhoons, high temporal resolution data in the upper ocean are required. In this study, the HYCOM reanalysis data are applied to obtain the near-inertial currents and NIKE induced by 12 different typhoons. The spatial and temporal resolutions of the HYCOM reanalysis data are 3 h and approximately  $0.08^\circ$ , respectively, which provide sea surface height, water temperature, salinity and two components of current velocity. The atmospheric forcing for the HYCOM reanalysis model comes from the hourly CFSR Reanalysis product.

### 2.5. SLOSH Model

In this study, a numerical-dynamic, tropical storm surge model, SLOSH (Sea, Land, and Overland Surges from Hurricanes) [50] is adopted to simulate an idealized typhoon. The wind speed of a typhoon is defined as,

$$V = V_{\max} \frac{2R R_{\max}}{R_{\max}^2 + R^2}, \quad (6)$$

where  $V_{\max}$  is the maximum wind speed at the radius  $R_{\max}$ , and  $R$  is the distance to the center of the typhoon. Following Zhang et al. [51], we adjust the wind field to the standard 10 m elevation by Equation (7), then the wind speed is projected to inflow direction and a correction term is used to get an asymmetry wind field by using Equation (8),

$$V_{10} = K_c K_m V, \quad (7)$$

$$U(r) = \frac{R_{\max} R}{R_{\max}^2 + R^2} U_T, \quad (8)$$

where  $K_m = 0.8$  is the correction factor [52] and  $K_c = 0.92$  is a factor to convert the sustained wind field to an hourly average [53].  $U_T$  is the translation speed of the typhoon (more detailed description can be seen in Zhang et al. [51]).

## 3. Results and Discussion

### 3.1. Observed NIWS and Oceanic Near-Inertial Current in Typhoon

A category 4 tropical cyclone, Neoguri, and two category 2 tropical cyclones, Mekkhala and Higos, passed by the meteorological observation station at Xisha Islands in 2008 (Figure 1). The wind speed recorded by the meteorological sensor was averaged every 1 hour. A Butterworth band-pass filter with a frequency range of  $0.85\text{--}1.15f$  [28] was applied to the wind stress to extract the NIWS. As shown in Figure 2, both the wind stress and NIWS were significantly increased when Neoguri (Figure 1) passed by the observation station, while Mekkhala and Higos excited much less increases in the magnitudes of NIWS. It shows that different categories and intensities of a tropical cyclone can induce diverse intensities of NIWS. Then, we apply the wind stress and NIWS to the slab model to compare the magnitudes of corresponding oceanic near-inertial currents in the mixed layer.

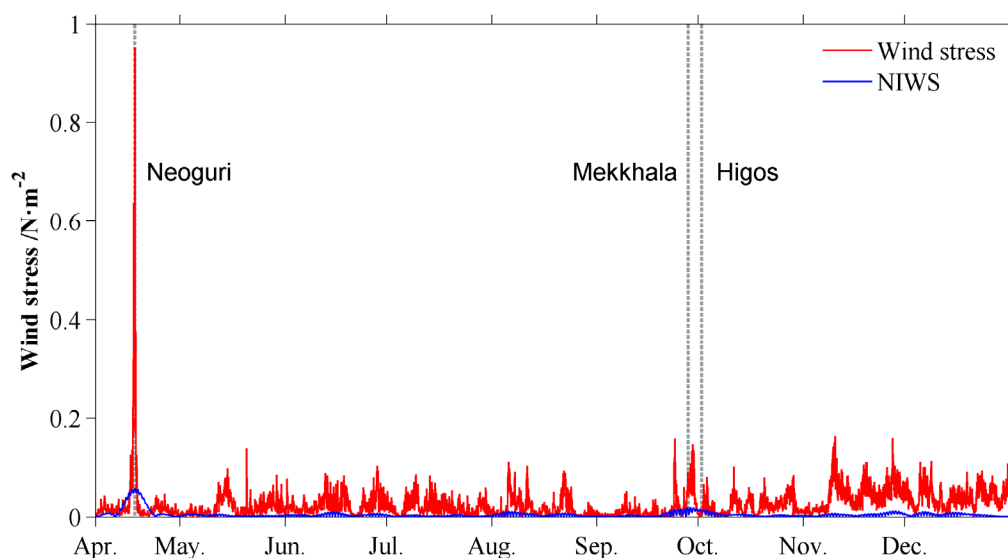


**Figure 2.** Time series of the hourly wind stress (red line, unit in  $\text{N}/\text{m}^2$ ) and near-inertial wind stress (NIWS, blue line) at the meteorological observation station from 6 April to 31 December in 2008. Vertical dashed lines denote the arrival of typhoons.

Figure 3 shows the variations of eastward and northward components of oceanic near-inertial current in the mixed layer from 6 April to 31 May. Before the arrival of Typhoon Neoguri on 17 April, the near-inertial currents do not match well with the wind stress, which may be due to the instabilities of the slab model and the filter at the initial stage. From 17 April, the variations of two currents are consistent with each other, and the time-integrated NIKE induced by NIWS contributes to about 80% of the NIKE induced by the typhoon from 17 April to 21 April, while the remaining 20% of NIKE may attribute to other effects. Hence, to a large extent, the typhoon-induced near-inertial currents are primarily induced by the NIWS in the typhoon.

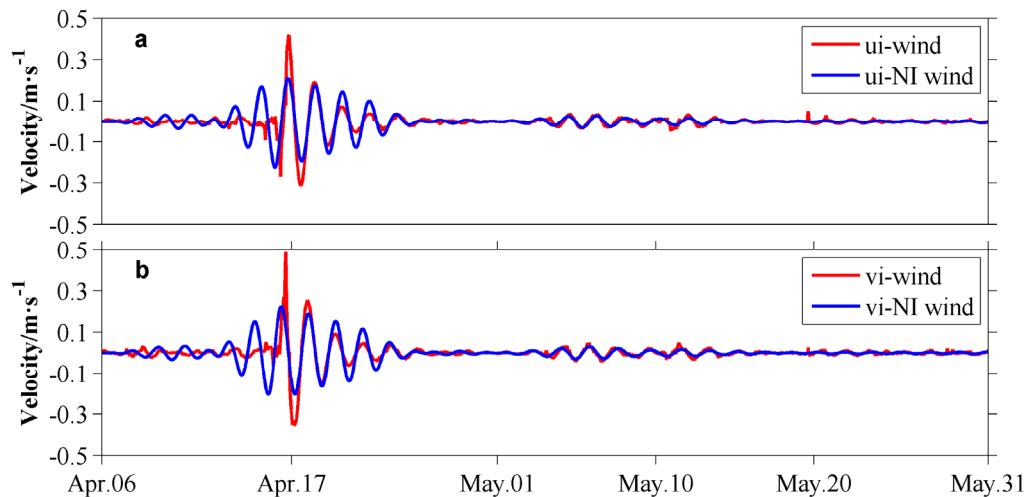


**Figure 3.** Components of the oceanic near-inertial current (unit in m/s) induced by wind stress (red lines) and the NIWS (blue lines) of Typhoon Neoguri at the observing station in April and May.

### 3.2. Oceanic NIKE Induced by 12 Typhoons and the Corresponding NIWS

In this study, we choose 12 actual typhoons to investigate the correlation of NIWS with NIKE in typhoons, and the tracks are shown in Figure 1 (denoted by yellow dots). The 12 typhoons have some common characteristics in path and background wind field. The HYCOM and CFSR reanalysis data are used to display the oceanic and atmospheric response to the 12 typhoons. The surface distributions of 3-day averaged NIKE during the passages of 12 typhoons are shown in Figure 4. It shows that although the typhoons have similar paths and backgrounds, the typhoon-induced NIKE varies greatly, e.g., Typhoon Imbudo excites the largest NIKE (Figure 4e) in the upper SCS, while Yutu (Figure 4a) and Molave (Figure 4b) induce much less NIKE. Meanwhile, notable rightward biases and small coastal near-inertial energy are shown in Figure 4. The small coastal NIKE is well-documented in the previous studies and always due to the confined propagation near the coastal area and the shallow water depth [54–56].

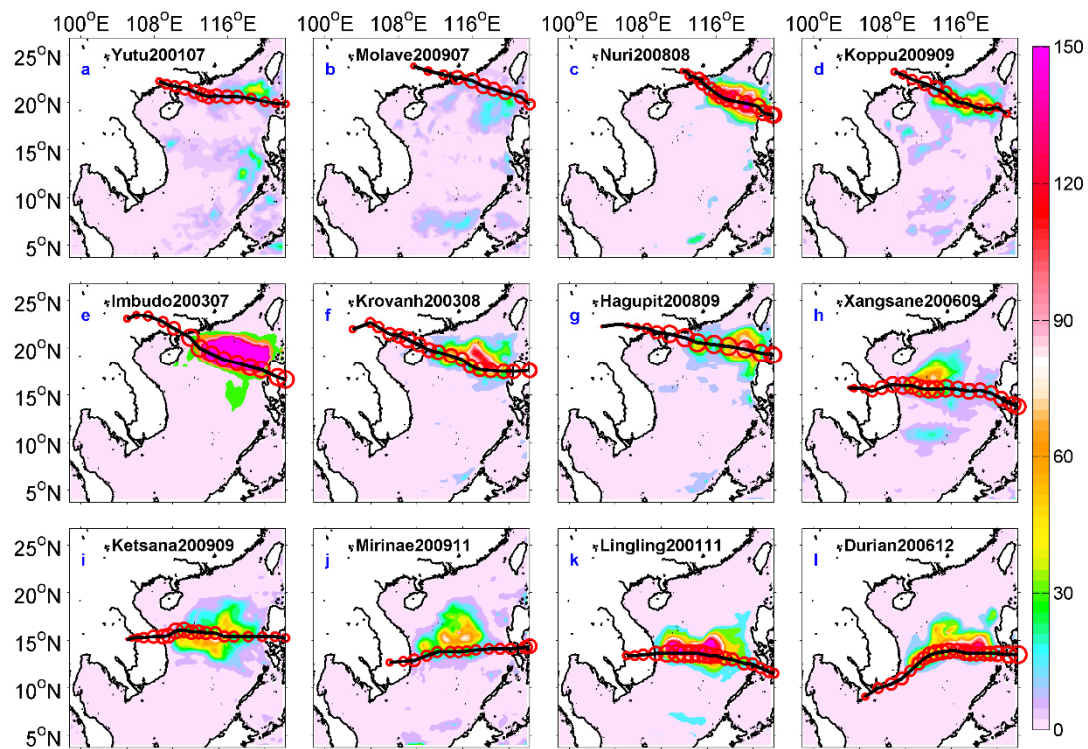


**Figure 4.** Typhoon tracks and surface 3-day averaged near-inertial kinetic energy (NIKE) (unit in  $J/m^3$ ), filtered from the Hybrid Coordinate Ocean Model (HYCOM) reanalysis data when Typhoons Yutu (a), Molave (b), Nuri (c), Koppu (d), Imbudo (e), Krovanh (f), Hagupit (g), Xangsane (h), Ketsana (i), Mirinae (j), Lingling (k), and Durian (l) passed over the South China Sea (SCS). Here, and subsequently, the red circles indicate the position of the typhoon center every 6 hours, and the size of the circle indicates the magnitude of the typhoon speed.

Comparing to NIKE distributions, the corresponding distributions of NIWS are shown in Figure 5. The NIWS is filtered from the wind stress of CFSR data with a frequency range of  $0.85\text{--}1.15f$ , and averaged over three days during the passages of typhoons. The intensities and distributions of NIWS in most typhoons are consistent with the magnitudes and features of NIKE, e.g., the NIWS in Typhoon Imbudo is the largest and a significant rightward bias appears on the right side of the track (Figure 5e). However, in some coastal areas, the NIKE presents some mismatches with the corresponding NIWS, which is presumably due to the complicated boundary.

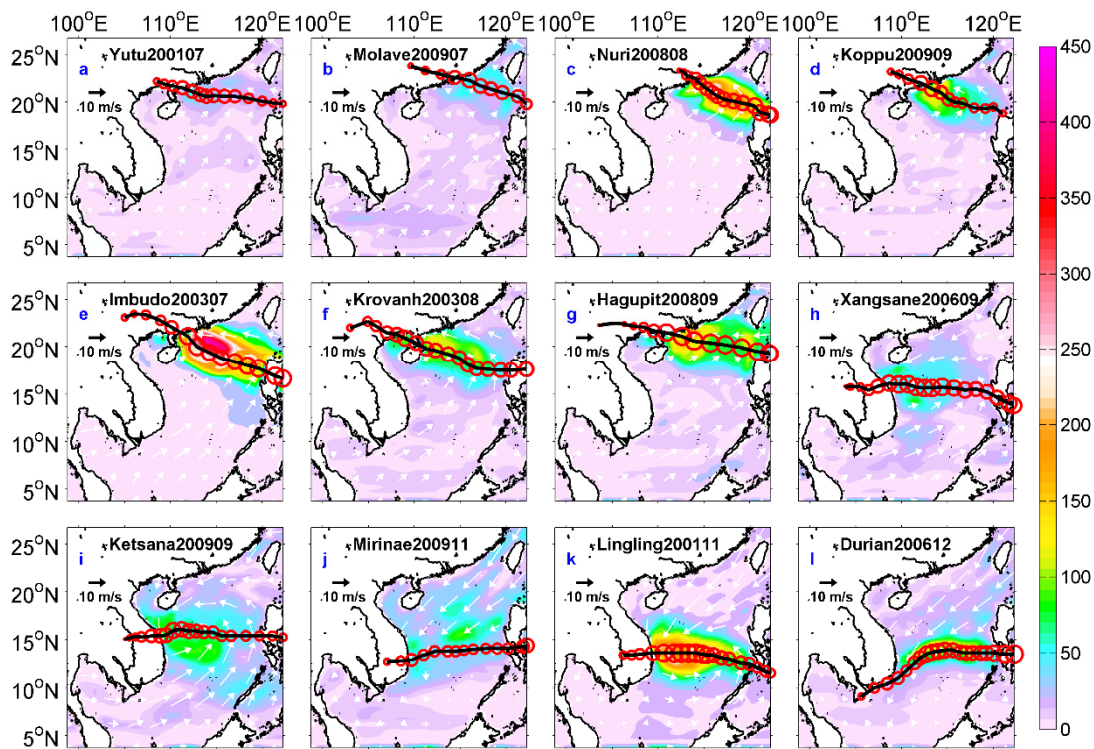


**Figure 5.** Typhoon tracks and 3-day averaged NIWS (unit in  $10^{-3} \text{ N/m}^2$ ), filtered from wind stress of Climate Forecast System Reanalysis (CFSR) data when Typhoons Yutu (a), Molave (b), Nuri (c), Koppu (d), Imbudo (e), Krovanh (f), Hagupit (g), Xangsane (h), Ketsana (i), Mirinae (j), Lingling (k), and Durian (l) passed over the SCS. The white arrows are the background wind speeds.

### 3.3. Relationship among NIKE, NIWS and Typhoon Parameters

Oceanic response to a typhoon is usually examined through investigating the external parameters of a typhoon, e.g., translation speed, radius of maximum wind speed (size), occurring latitude, maximum wind speed, etc. [13,19,57–59]. As noted, the magnitude and rotary frequency of wind speed play critical roles in determining the intensity of oceanic near-inertial response [18]. Based on the reanalysis data, we focused on two primary independent parameters of typhoon, i.e., maximum wind speed and translation speed, and have some statistics of the 12 typhoons. The scatter plots of maximum wind speed along the typhoon track and the translation speed of the typhoon against the corresponding NIWS and NIKE are shown in Figure 6a–d. Note that  $p$ -value  $< 0.001$  means a significant linear regression relationship exists. It shows that the maximum wind speed has a positive correlation with NIWS and NIKE (Figure 6a,c), but the translation speed does not exhibit a distinct correlation with NIWS and NIKE (Figure 6b,d). The scatter plot in Figure 6e presents a quantitative correlation between NIKE and the corresponding NIWS. The multiple correlation coefficient reaches about 0.33, which indicates a good correlation between NIKE and the corresponding NIWS in the 12 typhoons.

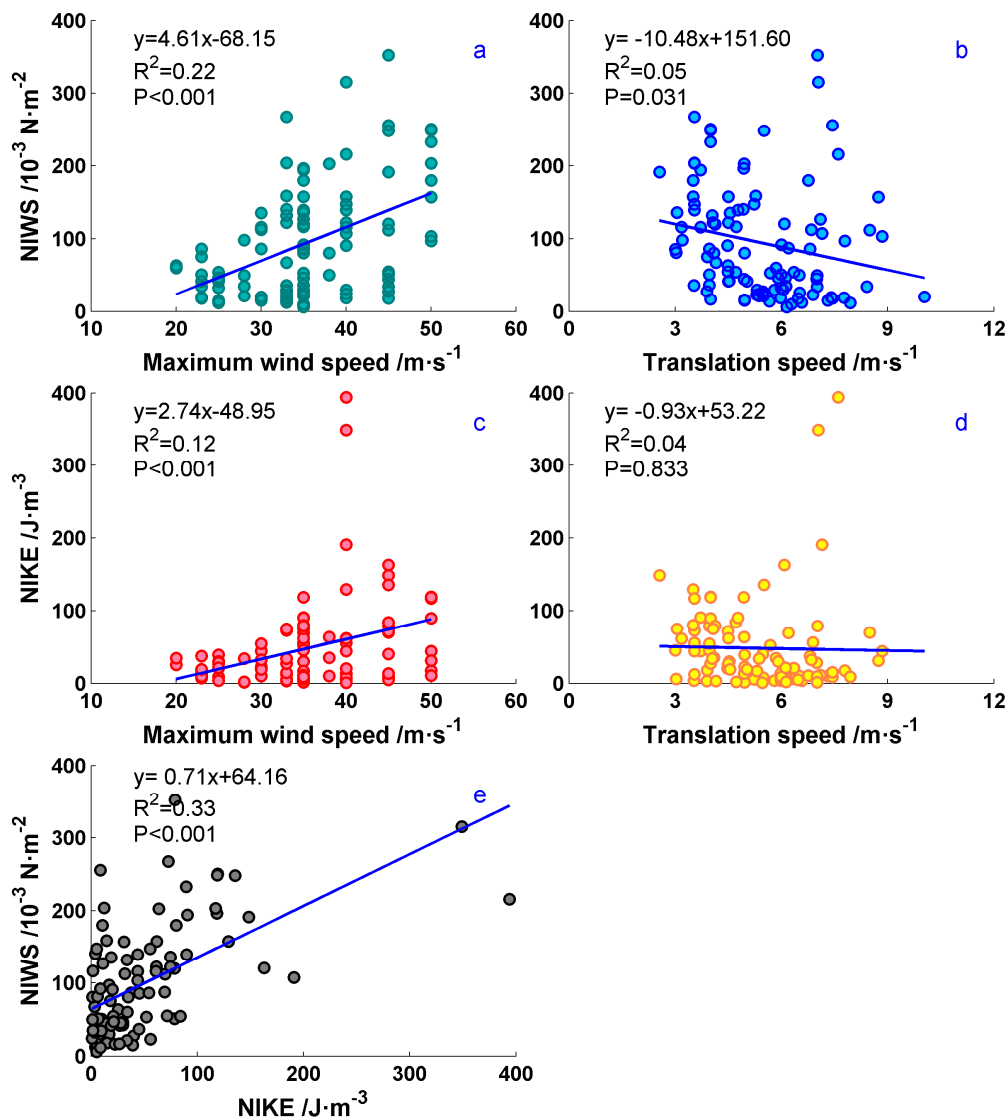


**Figure 6.** Scatter plots of maximum wind speed (unit in m/s) around the typhoon center and translation speed (unit in m/s) of typhoon versus the corresponding (a,b) NIWS (unit in  $10^{-3} \text{ N/m}^2$ ) and (c,d) NIKE (unit in  $\text{J/m}^3$ ) of 12 typhoons. (e) Scatter plot of NIKE against the corresponding NIWS.

### 3.4. Validation of Typhoon Model

To further examine the relationship between typhoon parameters and near-inertial motions, an idealized typhoon is established by the SLOSH model. The model domain is within ( $105^\circ \text{ E} \sim 161^\circ \text{ E}$ ,  $2^\circ \text{ N} \sim 29.1^\circ \text{ N}$ ). The grid size of the model used in this study is  $401 \times 201$  with a horizontal resolution of 15 km. The time step is set to 1 h, and the model is run for 400 h (Figure 7a). The ocean is initially at rest and horizontally homogeneous. The maximum wind speed ( $V_{\text{max}}$ ), translation speed ( $U_T$ ), and the radius  $R_{\text{max}}$  used in the SLOSH model are 25 m/s, 6 m/s, and 150 km, respectively. The wind field of the idealized typhoon at  $t = 150 \text{ h}$ , the corresponding NIWS, and oceanic near-inertial currents are shown in Figure 7. Here, the components of NIWS are extracted by a fourth-order Butterworth filter with a frequency range of  $0.85 \sim 1.15f$  in the time domain following [39], and the slab model is applied to obtain the mixed layer near-inertial currents. The mixed layer depth ( $H$ ) here is set as 50 m. In Figure 7, both of the NIWS and oceanic near-inertial currents show notable asymmetries along the typhoon track. A cluster of high-value centers of NIWS appear along the typhoon track, but there is only one high-value center for the near-inertial currents.

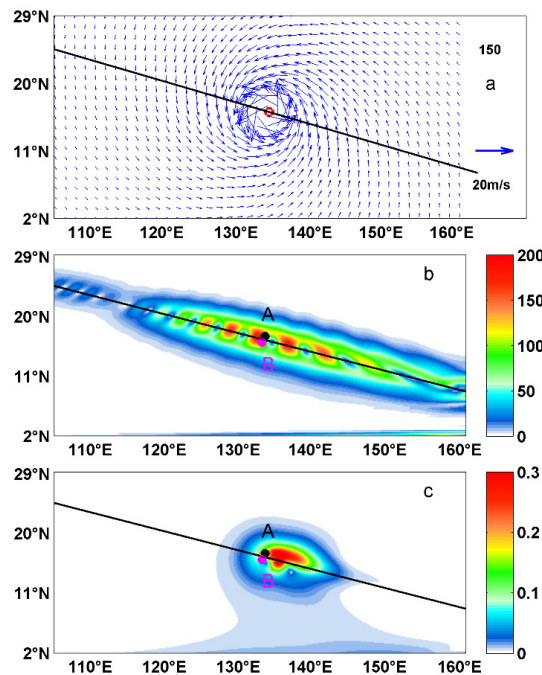


**Figure 7.** Distributions of (a) the wind field (unit in m/s) of the idealized typhoon at  $t = 150$  h, (b) corresponding NIWS (unit in  $10^{-3}$  N/m<sup>2</sup>), and (c) oceanic near-inertial currents (unit in m/s). The black line denotes the typhoon track. The red circle in (a) denotes the typhoon center. The black dot A in (b) and the magenta dot B in (c) are opposite locations on the two sides of the typhoon track.

To validate the model, a point ( $16^{\circ}85' N$ ,  $133.7^{\circ} E$ ) on the right side of the idealized typhoon (the black dot A shown in Figure 7b,c), which is about 80 km away from the typhoon track, was chosen to represent the meteorological observation station. The simulated wind speed at this location and the corresponding mixed layer near-inertial currents simulated from the slab model were compared with the observational data ( $16^{\circ}83' N$ ,  $112^{\circ}33' E$ ) and the CFSR data ( $16^{\circ}25' N$ ,  $112^{\circ}75' E$ ), respectively (Figure 8). It shows that the SLOSH model results basically match the observations.

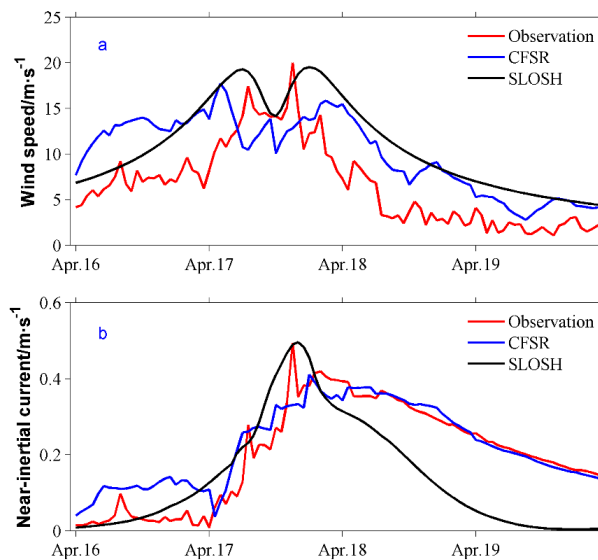


**Figure 8.** Comparison of (a) observed wind speed (unit in m/s, red line), CFSR wind speed (blue line), and idealized surface wind speed by SLOSH model (black line) when Typhoon Neoguri passed by the Xisha observation station from April 16 to April 19. (b) Same as in (a), but for the corresponding mixed layer near-inertial currents (unit in m/s).

### 3.5. Sensitivity Experiments and Analysis

As shown in Figure 6, the relationship between translation speed and NIWS is not clear. Here, based on the validated SLOSH model, nine numerical experiments were conducted to investigate the relationship between translation speed and NIWS (Table 1). Case 1 is the standard experiment validated in Section 3.4, and all numerical experiments were divided into two groups. Cases 1–5 are the experiments for the sensitivity of maximum wind speed ( $V_{max}$ ). Cases 1 and 6–9 are the experiments for the sensitivity of translation speed ( $U_T$ ). The variations of NIWS and oceanic near-inertial currents ( $U_i$ ) for the nine numerical experiments at location A are shown in Figure 9. When  $V_{max}$  increases from 15 m/s to 35 m/s, the maximum NIWS increases from  $48.6 \times 10^{-3} \text{ N/m}^2$  to  $352.2 \times 10^{-3} \text{ N/m}^2$  (Figure 9a), and the magnitude of oceanic near-inertial currents ( $U_i$ ) increases from about 0.1 m/s to 0.69 m/s (Figure 9c). When the translation speed ( $U_T$ ) increases from 4 m/s to 5 m/s, the maximum NIWS increases from  $152.5 \times 10^{-3} \text{ N/m}^2$  to  $176.2 \times 10^{-3} \text{ N/m}^2$ , but when the translation speed ( $U_T$ ) increases from 5 m/s to 8 m/s, the maximum NIWS decreases to  $154.6 \times 10^{-3} \text{ N/m}^2$  (Figure 9b), and the corresponding  $U_i$  increases from 0.24 m/s to 0.39 m/s, monotonically (Figure 9d).

**Table 1.** Design of numerical experiments. Case 1 is the standard experiment.  $V_{max}$  is the maximum wind speed at the radius  $R_{max}$ ;  $U_T$  is the translation speed of the typhoon.

Experiment	Case1	Case2	Case3	Case4	Case5	Case6	Case7	Case8	Case9
$V_{max}$ (m/s)	25	15	20	30	35	25	25	25	25
$U_T$ (m/s)	6	6	6	6	6	4	5	7	8

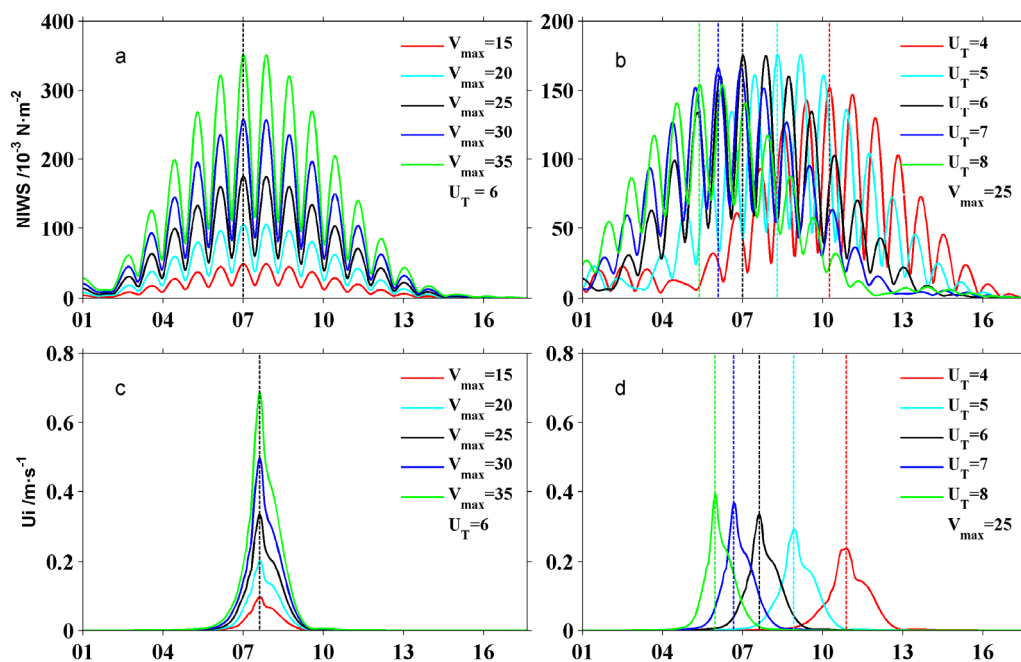


**Figure 9.** Time series (in days) of NIWS (unit  $10^{-3} \text{ N/m}^2$ ) and oceanic near-inertial currents  $U_i$  (unit in m/s) in the mixed layer of fixed location A. (a,c) are the experiment results for the sensitivity of maximum wind speed ( $V_{max}$ ). (b,d) are the experiment results for the sensitivity of translation speed ( $U_T$ ).

It shows that the maximum near-inertial current increases with the translation speed monotonically, but the maximum NIWS may vary parabolically with the translation speeds, and it reaches the maximum at  $U_T = 5 \text{ m/s}$  (denoted by “optimal translation speed” hereafter). As noted, at the forced stage, the maximum oceanic near-inertial energy monotonically increases with the translation speed of the typhoon [18], while at the relaxation stage of inertial process, the amplitude of the oceanic near-inertial energy always presents an optimal turn with the translation speed [17,18], which exhibits a similar

characteristic to NIWS. On the other hand, according to the comparison of observation in Section 3.1, the time-integrated NIKE induced by NIWS contributes to about 80% of the NIKE induced by the typhoon, and the rest of NIKE may contribute to other effects. This may explain why the maximum near-inertial current increases with the increasing translational speed, while the NIWS does not. Moreover, there is a time lag between the maximum near-inertial current and maximum NIWS. The maximum NIWS arrives about 15 hours prior to the maximum near-inertial current, which is comparable with the observational result by Xu et al. [59].

To further investigate the optimal translation speed for the NIWS, the power spectral densities (PSDs) of the wind stress at location A are shown in Figure 10. It was found that both the wind energies at the synoptic band ( $S_1$ – $S_2$ , with periods of 2–6 days) and near-inertial band ( $f_1$ – $f_2$ , i.e.,  $0.85$ – $1.15f$ , with periods of 36–48.7 h) are much larger than those at diurnal ( $D_1$ , with a period of 24 h) and semidiurnal frequencies ( $D_2$ , with a period of 12 h). Comparing to the eastward components, the northward components of wind energy at the near-inertial band greatly vary with the translation speed ( $U_T$ ). The curves show that the smaller translation speed (e.g.,  $U_T = 4$  m/s) contributes more energy at the relatively low frequency (e.g., at synoptic band), while the larger translation speed (e.g.,  $U_T = 8$  m/s) contributes more energy at the relatively high frequency (e.g., at diurnal frequency). These processes lead to the occurrence of the largest near-inertial-band PSD at  $U_T = 5$  m/s.

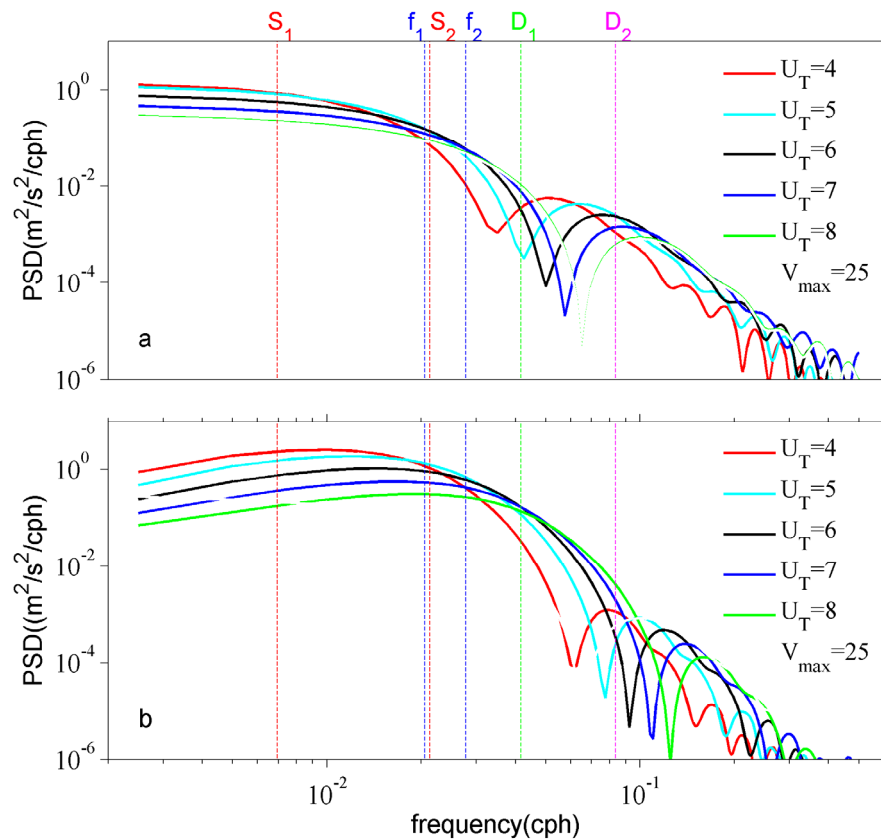


**Figure 10.** Power spectral densities (PSDs) of (a) eastward components and (b) northward components of wind stress at location A (solid lines). The blue dashed lines indicate the range of filtered near-inertial frequency band ( $f_1$ – $f_2$ ). The red dashed lines indicate the range of synoptic frequency band ( $S_1$ – $S_2$ ). The green and magenta dashed lines denote the diurnal ( $D_1$ ) and semidiurnal ( $D_2$ ) frequencies, respectively.

The structures of typhoon and oceanic response are always asymmetric. Here, the variations of NIWS and oceanic near-inertial currents ( $U_i$ ) on the left side of the cyclone track (location B in Figure 7b,c) are shown in Figure 11. The magnitudes of NIWS in different cases are smaller than those at location A, and numerical differences may promote the asymmetry of the oceanic near-inertial

response to typhoon. The optimal translation speed for the NIWS also appears at  $U_T = 5$  m/s. The PSDs of the wind stress at location B are displayed in Figure 12. The variation trend and the PSDs of northward components are similar to those at location A, but the PSDs of eastward components are much smaller than those at location A. It is inferred that the smaller magnitude of NIWS on the left side of the track is mainly due to the smaller energy of the eastward component at the near-inertial band.

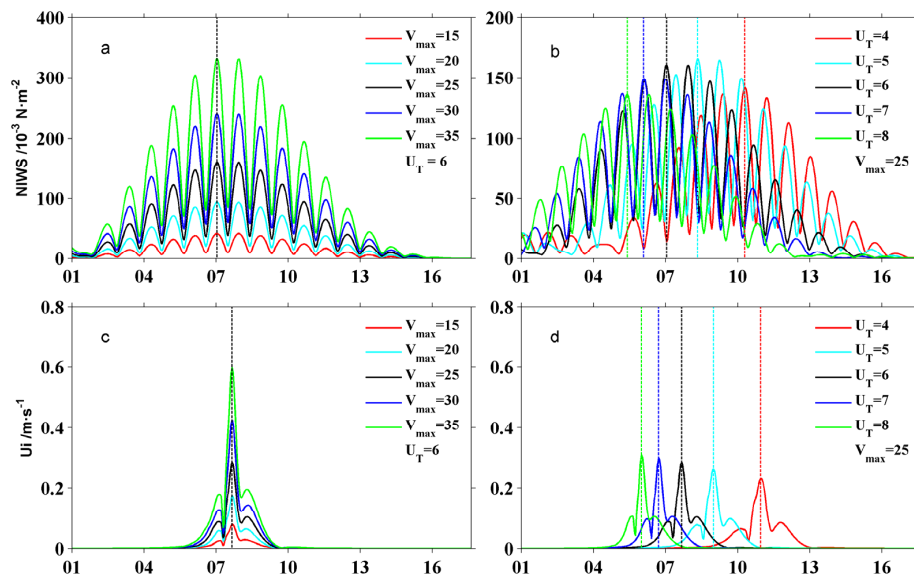


**Figure 11.** Time series (in days) of NIWS (unit  $10^{-3}$  N/m<sup>2</sup>) and oceanic near-inertial currents  $U_i$  (unit in m/s) in the mixed layer of fixed location B. (a,c) are the experiment results for the sensitivity of maximum wind speed ( $V_{max}$ ). (b,d) are the experiment results for the sensitivity of translation speed ( $U_T$ ).

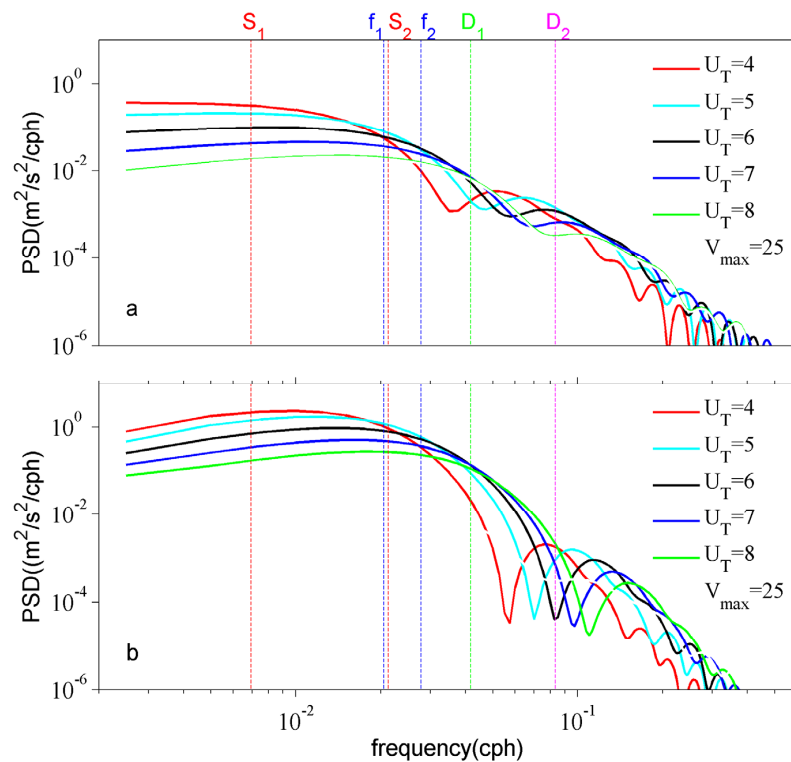


**Figure 12.** Power spectral densities (PSDs) of (a) eastward components and (b) northward components of wind stress at location B (solid lines). The blue dashed lines indicate the range of filtered near-inertial frequency band ( $f_1$ – $f_2$ ). The red dashed lines indicate the range of synoptic frequency band ( $S_1$ – $S_2$ ). The green and magenta dashed lines denote the diurnal ( $D_1$ ) and semidiurnal ( $D_2$ ) frequencies, respectively.

#### 4. Conclusions

Strong atmospheric forcing of a typhoon can induce strong near-inertial currents in the upper ocean. The relationship between NIWS, typhoon-induced oceanic near-inertial currents, and typhoon parameters was investigated through reanalysis data and an idealized typhoon model. The main conclusions are as follows:

The oceanic near-inertial currents are primarily induced by the NIWS in a typhoon, which may contribute to about 80% of the total NIKE induced by a typhoon. According to the reanalysis data and a series of numerical experiments in the SLOSH typhoon model, the intensities and distributions of NIWS in most of typhoons are consistent with the magnitudes and features of NIKE. Two primary parameters of typhoon, i.e., maximum wind speed and translation speed, play key roles in determining the magnitudes of NIWS and near-inertial energy. It was found that the NIWS and the NIKE along the typhoon track have positive correlations with the maximum wind speeds of the typhoon. The maximum oceanic near-inertial currents increase with the translation speeds, but the maximum NIWS may vary parabolically with the translation speeds. There is an optimal translation speed for the NIWS, at which the wind energy of the near-inertial band reaches its maximum.

On the other hand, a cluster of high-value centers of NIWS appear along the typhoon track, but there is only one high-value center for the near-inertial currents. There is a time lag between the maximum NIWS and maximum near-inertial current. The maximum NIWS arrives about 15 h prior to the maximum near-inertial current. The distribution of NIWS is apparently asymmetric along the typhoon track, which may be due to the smaller eastward component of wind energy, and it may promote the asymmetry of the oceanic near-inertial response to typhoons.

**Author Contributions:** Conceptualization, J.L. (Juan Li) and S.C.; Formal analysis, J.L. (Juan Li), Z.C., and S.C.; Data Curation, J.L. (Junliang Liu) and J.X.; Methodology, J.L. (Juan Li), J.X., and Y.H.; Validation, J.L. (Juan Li); Funding Acquisition, J.L. (Junliang Liu), Z.C., and S.C.; Writing—Original Draft, J.L. (Juan Li); Writing—Review and Editing, J.L. (Juan Li) and S.C.

**Funding:** This work is jointly supported by the Key Research Program of Frontier Sciences, Chinese Academy of Sciences (CAS) (No. QYZDJ-SSW-DQC034), National Natural Science Foundation of China Grants 41890851, 41430964, 41521005, 41776005, 41776007, 41406023 and 41476011, and No. ISEE2018PY05 from CAS, the Youth Innovation Promotion Association CAS (No. 2018378).

**Acknowledgments:** The NCEP/CFSR data were developed by NOAA's National Centers for Environmental Prediction (NCEP), which are available at <http://rda.ucar.edu/datasets/ds093.1>. The HYCOM reanalysis data are produced by the HYCOM Consortium (<https://hycom.org/dataserver/gofs-3pt0/reanalysis>). The tracks of TCs are contributed by the China Meteorological Administration (CMA)'s TC database (<http://tcdata.typhoon.org.cn/>). Acknowledgement for the meteorological observation data support from "South China Sea and Adjacent Seas Data Center, National Earth System Science Data Sharing Infrastructure, National Science and Technology Infrastructure of China (<http://ocean.geodata.cn>).” The authors also gratefully acknowledge the use of the computer HPCC for all numeric calculations and data analysis at the South China Sea Institute of Oceanology, Chinese Academy of Sciences.

**Conflicts of Interest:** The authors declare no conflict of interest.

#### References

1. Wunsch, C. The work done by the wind on the oceanic general circulation. *J. Phys. Oceanogr.* **1998**, *28*, 2332–2340. [[CrossRef](#)]
2. Wunsch, C.; Ferrari, R. Vertical mixing, energy, and the general circulation of the oceans. *Annu. Rev. Fluid Mech.* **2004**, *36*, 281–314. [[CrossRef](#)]
3. Ferrari, R.; Wunsch, C. Ocean circulation kinetic energy: Reservoirs, sources, and sinks. *Annu. Rev. Fluid Mech.* **2009**, *41*, 253–282. [[CrossRef](#)]
4. Zhai, X.; Johnson, H.L.; Marshall, D.P.; Wunsch, C. On the wind power input to the ocean general circulation. *J. Phys. Oceanogr.* **2012**, *42*, 1357–1365. [[CrossRef](#)]
5. Gill, A.E. On the behavior of internal waves in the wakes of storms. *J. Phys. Oceanogr.* **1984**, *14*, 1129–1151. [[CrossRef](#)]

6. Munk, W.; Wunsch, C. Abyssal recipes II: Energetics of tidal and wind mixing. *Deep Sea Res. Part I* **1998**, *45*, 1977–2010. [[CrossRef](#)]
7. Zhai, X.; Greatbatch, R.J.; Eden, C.; Hibiya, T. On the loss of wind-induced near-inertial energy to turbulent mixing in the upper ocean. *J. Phys. Oceanogr.* **2009**, *39*, 3040–3045. [[CrossRef](#)]
8. Xu, Z.; Yin, B.; Hou, Y.; Xu, Y. Variability of internal tides and near-inertial waves on the continental slope of the northwestern South China Sea. *J. Geophys. Res.* **2013**, *118*, 197–211. [[CrossRef](#)]
9. Jordi, A.; Wang, D.P. Estimation of wind forcing and analysis of near-inertial motions generated by a storm in a submarine canyon with an ensemble Kalman filter. *Cont. Shelf Res.* **2015**, *94*, 17–27. [[CrossRef](#)]
10. Xiao, J.; Xie, Q.; Wang, D.; Yang, L.; Shu, Y.; Liu, C.; Chen, J.; Yao, J.; Chen, G. On the near-inertial variations of meridional overturning circulation in the South China Sea. *Ocean Sci.* **2016**, *12*, 335–344. [[CrossRef](#)]
11. Liu, L.L.; Wang, W.; Huang, R.X. The mechanical energy input to the ocean induced by tropical cyclones. *J. Phys. Oceanogr.* **2008**, *38*, 1253–1266. [[CrossRef](#)]
12. Ginis, I. Tropical cyclone-ocean interactions. *Adv. Fluid Mech.* **2002**, *33*, 83–114.
13. Price, J.F.; Sanford, T.B.; Forristall, G.Z. Forced stage response to a moving hurricane. *J. Phys. Oceanogr.* **1994**, *24*, 233–260. [[CrossRef](#)]
14. Frank, W.M. The structure and energetics of the tropical cyclone I. Storm structure. *Mon. Weather Rev.* **1977**, *105*, 1119–1135. [[CrossRef](#)]
15. Sun, Z.; Hu, J.; Zheng, Q.; Gan, J. Comparison of typhoon-induced near-inertial oscillations in shear flow in the northern South China Sea. *Acta Oceanol. Sin.* **2015**, *34*, 38–45. [[CrossRef](#)]
16. Xie, X.H.; Shang, X.D.; Chen, G.Y.; Sun, L. Variations of diurnal and inertial spectral peaks near the bi-diurnal critical latitude. *Geophys. Res. Lett.* **2009**, *36*. [[CrossRef](#)]
17. Nilsson, J. Energy flux from travelling hurricanes to the oceanic internal wave field. *J. Phys. Oceanogr.* **1995**, *25*, 558–573. [[CrossRef](#)]
18. Chen, S.; Polton, J.A.; Hu, J.; Xing, J. Local inertial oscillations in the surface ocean generated by time-varying winds. *Ocean Dyn.* **2005**, *65*, 1633–1641. [[CrossRef](#)]
19. Xie, L.; Liu, H.; Liu, B.; Bao, S. A numerical study of the effect of hurricane wind asymmetry on storm surge and inundation. *Ocean Model.* **2011**, *36*, 71–79. [[CrossRef](#)]
20. Chang, S.W.; Anthes, R.A. Numerical simulations of the ocean's nonlinear, baroclinic response to translating hurricanes. *J. Phys. Oceanogr.* **1978**, *8*, 468–480. [[CrossRef](#)]
21. Shapiro, L. The asymmetric boundary layer flow under a translating hurricane. *J. Atmos. Sci.* **1983**, *40*, 1984–1998. [[CrossRef](#)]
22. Wang, Y.; Holland, G.J. Tropical cyclone motion and evolution in vertical shear. *J. Atmos. Sci.* **1996**, *53*, 3313–3332. [[CrossRef](#)]
23. Ross, R.J.; Kurihara, Y. A simplified scheme to simulate asymmetries due to the beta effect in barotropic vortices. *J. Atmos. Sci.* **1992**, *49*, 1620–1628. [[CrossRef](#)]
24. Chen, S.; Hu, J.; Polton, J.A. Features of near-inertial motions observed on the northern South China Sea shelf during the passage of two typhoons. *Acta Oceanol. Sin.* **2015**, *34*, 38–43. [[CrossRef](#)]
25. Price, J.F. Upper ocean response to a hurricane. *J. Phys. Oceanogr.* **1981**, *11*, 153–175. [[CrossRef](#)]
26. Sun, L.; Zheng, Q.; Wang, D.; Hu, J.; Tai, C.K.; Sun, Z. A case study of near-inertial oscillation in the South China Sea using mooring observations and satellite altimeter data. *J. Oceanogr.* **2011**, *67*, 677–687. [[CrossRef](#)]
27. Sun, L.; Zheng, Q.A.; Tang, T.Y.; Chuang, W.S.; Li, L.; Hu, J.; Wang, D. Upper ocean near-inertial response to 1998 Typhoon Faith in the South China Sea. *Acta Oceanol. Sin.* **2012**, *31*, 25–32. [[CrossRef](#)]
28. Chen, G.; Xue, H.; Wang, D.; Xie, Q. Observed near-inertial kinetic energy in the northwestern South China Sea. *J. Geophys. Res.* **2013**, *118*, 4965–4977. [[CrossRef](#)]
29. Lin, F.; Liang, C.; Hou, Y.; Liu, Y.; Liu, Z.; Hu, P. Observation of interactions between internal tides and near-inertial waves after typhoon passage in the northern South China Sea. *Chin. J. Oceanol. Limnol.* **2015**, *33*, 1279–1285. [[CrossRef](#)]
30. Ding, W.; Liang, C.; Liao, G.; Li, J.; Lin, F.; Jin, W.; Zhu, L. Propagation characteristics of near-inertial waves along the continental shelf in the wake of the 2008 Typhoon Hagupit in the northern South China Sea. *Bull. Mar. Sci.* **2018**, *94*, 1293–1311. [[CrossRef](#)]
31. Wu, R.; Zhang, H.; Chen, D.; Li, C.; Lin, J. Impact of Typhoon Kalmaegi (2014) on the South China Sea: Simulations using a fully coupled atmosphere-ocean-wave model. *Ocean Model.* **2018**, *131*, 132–151. [[CrossRef](#)]

32. Liu, J.; Cai, S.; Wang, S. Observations of strong near-bottom current after the passage of typhoon pabuk in the south china sea. *J. Mar. Syst.* **2011**, *87*, 102–108. [[CrossRef](#)]
33. Cao, A.; Guo, Z.; Song, J.; Lv, X.; He, H.; Fan, W. Near-Inertial Waves and Their Underlying Mechanisms Based on the South China Sea Internal Wave Experiment (2010–2011). *J. Geophys. Res.* **2018**, *123*, 5026–5040. [[CrossRef](#)]
34. Crawford, G.B.; Large, W.G. A numerical investigation of resonant inertial response of the ocean to wind forcing. *J. Phys. Oceanogr.* **1996**, *26*, 873–891. [[CrossRef](#)]
35. Zhai, X. Latitudinal dependence of wind-induced near-inertial energy. *J. Phys. Oceanogr.* **2015**, *45*, 3025–3032. [[CrossRef](#)]
36. Ying, M.; Zhang, W.; Yu, H.; Lu, X.; Feng, J.; Fan, Y.; Zhu, Y.; Chen, D. An overview of the China Meteorological Administration tropical cyclone database. *J. Atmos. Ocean. Technol.* **2014**, *31*, 287–301. [[CrossRef](#)]
37. Saha, S.; Moorthi, S.; Pan, H.L.; Wu, X.; Wang, J.; Nadiga, S.; Zou, C.-Z.; Liu, Q.; Chen, Y.; Liu, H.; et al. The NCEP climate forecast system reanalysis. *Bull. Am. Meteorol. Soc.* **2010**, *91*, 1015–1058. [[CrossRef](#)]
38. Oey, L.Y.; Ezer, T.; Wang, D.P.; Fan, S.J.; Yin, X.Q. Loop current warming by Hurricane Wilma. *Geophys. Res. Lett.* **2006**, *33*. [[CrossRef](#)]
39. Guan, S.; Zhao, W.; Huthnance, J.; Tian, J.; Wang, J. Observed upper ocean response to typhoon Megi (2010) in the Northern South China Sea. *J. Geophys. Res.* **2014**, *119*, 3134–3157. [[CrossRef](#)]
40. Large, W.G.; Pond, S. Open ocean momentum flux measurements in moderate to strong winds. *J. Phys. Oceanogr.* **1981**, *11*, 324–336. [[CrossRef](#)]
41. Powell, M.D.; Vickery, P.J.; Reinhold, T.A. Reduced drag coefficient for high wind speeds in tropical cyclones. *Nature* **2003**, *422*, 279. [[CrossRef](#)] [[PubMed](#)]
42. Dippe, T.; Zhai, X.; Greatbatch, R.J.; Rath, W. Interannual variability of wind power input to near-inertial motions in the North Atlantic. *Ocean Dyn.* **2015**, *65*, 859–875. [[CrossRef](#)]
43. Pollard, R.T.; Millard, R.C. Comparison between observed and simulated wind-generated inertial oscillations. *Deep-Sea Res. Oceanogr. Abstr.* **1970**, *17*, 813–816. [[CrossRef](#)]
44. Alford, M.H. Internal swell generation: The spatial distribution of energy flux from the wind to mixed layer near-inertial motions. *J. Phys. Oceanogr.* **2001**, *31*, 2359–2368. [[CrossRef](#)]
45. Monterey, G.; Levitus, S. *Seasonal Variability of Mixed Layer Depth for the World Ocean*; NOAA Atlas NESDIS 14; National Oceanic and Atmospheric Administration: Silver Spring, MD, USA, 1997; 100p.
46. Fox, D.N.; Teague, W.J.; Barron, C.N.; Carnes, M.R.; Lee, C.M. The modular ocean data assimilation system (MODAS). *J. Atmos. Ocean. Technol.* **2002**, *19*, 240–252. [[CrossRef](#)]
47. Cummings, J.A. Operational multivariate ocean data assimilation. *Quart. J. R. Met. Soc. Part C* **2005**, *131*, 3583–3604. [[CrossRef](#)]
48. Cummings, A.J.; Smedstad, O.M. Variational Data Assimilation for the Global Ocean. In *Data Assimilation for Atmospheric, Oceanic and Hydrologic Applications*; Springer: Berlin/Heidelberg, Germany, 2013; Volume II, Chapter 13; pp. 303–343.
49. D’Asaro, E.A. The energy flux from the wind to near-inertial motions in the surface mixed layer. *J. Phys. Oceanogr.* **1985**, *15*, 1043–1059. [[CrossRef](#)]
50. Jelesnianski, C.P. Numerical computation of storm surges without bottom stress. *Mon. Weather Rev.* **1966**, *94*, 374–379. [[CrossRef](#)]
51. Zhang, H.; Chen, D.; Zhou, L.; Liu, X.; Ding, T.; Zhou, B. Upper ocean response to typhoon Kalmaegi (2014). *J. Geophys. Res.* **2016**, *121*, 6520–6535. [[CrossRef](#)]
52. Powell, M.D.; Black, P.G. The relationship of hurricane reconnaissance flight-level wind measurements to winds measured by NOAA’s oceanic platforms. *J. Wind Eng. Ind. Aerodyn.* **1990**, *36*, 381–392. [[CrossRef](#)]
53. Krayner, W.R.; Marshall, R.D. Gust factors applied to hurricane winds. *Bull. Am. Meteorol. Soc.* **1992**, *73*, 613–618. [[CrossRef](#)]
54. Anderson, I.; Huyer, A.; Smith, R.L. Near-inertial motions off the Oregon coast. *J. Geophys. Res.* **1983**, *88*, 5960–5972. [[CrossRef](#)]
55. Chen, C.; Reid, R.O.; Nowlin, W.D., Jr. Near-inertial oscillations over the Texas-Louisiana shelf. *J. Geophys. Res.* **1996**, *101*, 3509–3524. [[CrossRef](#)]
56. Chen, S.; Chen, D.; Xing, J. A study on some basic features of inertial oscillations and near-inertial internal waves. *Ocean Sci.* **2017**, *13*, 829–836. [[CrossRef](#)]

57. Greatbatch, R.J. On the response of the ocean to a moving storm: Parameters and scales. *J. Phys. Oceanogr.* **1984**, *14*, 59–78. [[CrossRef](#)]
58. Rayson, M.D.; Ivey, G.N.; Jones, N.L.; Lowe, R.J.; Wake, G.W.; McConochie, J.D. Near-inertial ocean response to tropical cyclone forcing on the Australian North-West Shelf. *J. Geophys. Res.* **2015**, *120*, 7722–7751. [[CrossRef](#)]
59. Xu, J.; Huang, Y.; Chen, Z.; Liu, J.; Liu, T.; Li, J.; Cai, S.; Ning, D. Horizontal variations of typhoon-forced near-inertial oscillations in the south China sea simulated by a numerical model. *Cont. Shelf Res.* **2019**, *39*, 1318–1323. [[CrossRef](#)]



© 2019 by the authors. Licensee MDPI, Basel, Switzerland. This article is an open access article distributed under the terms and conditions of the Creative Commons Attribution (CC BY) license (<http://creativecommons.org/licenses/by/4.0/>).